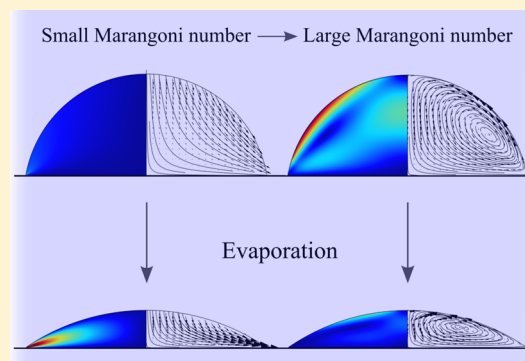


Convective Flows in Evaporating Sessile Droplets

Meysam R. Barmi and Carl D. Meinhardt*

Department of Mechanical Engineering, University of California Santa Barbara, Santa Barbara, California 93106, United States

ABSTRACT: The evaporation rate and internal convective flows of a sessile droplet with a pinned contact line were formulated and investigated numerically. We developed and analyzed a unified numerical model that includes the effects of temperature, droplet volume, and contact angle on evaporation rate and internal flows. The temperature gradient on the air/liquid interface causes an internal flow due to Marangoni stress, which provides good convective mixing within the droplet, depending upon Marangoni number. As the droplet volume decreases, the thermal gradient becomes smaller and the Marangoni flow becomes negligible. Simultaneously, as the droplet height decreases, evaporation-induced flow creates a large jet-like flow radially toward the contact line. For a droplet containing suspended particles, this jet-like convective flow carries particles toward the contact line and deposits them on the surface, forming the so-called “coffee ring stain”. In addition, we reported a simple polynomial correlation for dimensionless evaporation time as a function of initial contact angle of the pinned sessile droplet which agrees well with the previous experimental and numerical results.



INTRODUCTION

Evaporating droplets and controlling of drying systems containing small particles have received significant attention for their many applications such as DNA or protein deposition,^{1–3} spray-cooling technology,⁴ particle self-assembly,⁵ colloid crystallization,⁶ painting, inkjet printing, carbon nanotube formation,⁷ chemical detection,⁸ and other biological or chemical applications. In recent years, several studies have been conducted on evaporating liquid droplets on heating substrates. The mass loss from an evaporating droplet can be calculated on the basis of the diffusion of the liquid vapor from the interface into the surrounding atmosphere. Due to the non-isothermal conditions on the air/liquid interface, the evaporative flux is higher near the contact line, which causes convection from the apex to the contact line. Marangoni flow occurs as a result of the surface tension gradient on the free surface of the droplet caused by the non-isothermal interface. The Marangoni flow stirs the droplet, leading to an efficient convective mixing within the droplet, and the convective flow toward the contact line carries particulate matter to the contact line at the end of evaporation, which forms the so-called “coffee ring stain”.^{9–12} There are various experimental approaches and mathematical formulations to characterize the evaporation rate from hydrophilic and hydrophobic sessile droplets.^{13–20} In most numerical approaches, analogies between diffusive concentration fields and electrostatic potential fields based on Laplace equations have been utilized assuming quasi-steady conditions for evaporation. Several correlations have been proposed previously to estimate evaporation rate.^{21–23} A variety of models and experimental methods have been developed to characterize Marangoni flow,^{24,25} convective flow toward the contact line by neglecting Marangoni

stresses,^{26–28} and also a change in the contact angle during the evaporation.²⁹ However, to date, a unified model of the evaporation process, internal flow field, and details of pattern formation after droplet drying has not yet been developed and analyzed.

In the current research, we formulated and investigated the evaporation dynamics of an axisymmetric sessile droplet on a horizontal isothermal substrate numerically. A numerical model was constructed to quantify the convective flows within the droplet based on the droplet shape, evaporation rate, ambient conditions, and various surface temperatures.

THEORY AND NUMERICAL SIMULATIONS

On the basis of the previous experimental observations, for an evaporating sessile droplet with a contact angle less than 90°, there are two primary phases of evaporation. In phase I, the contact angle decreases while the contact line remains pinned, whereas, in phase II, the contact line recedes while the contact angle remains nearly constant. Phase I typically accounts for about 90% of the total evaporation time. In an exemplary experiment reported by Hu et al., the contact line was fixed during the evaporation process until the contact angle decreased to an angle of approximately 2–4°, at which point the contact line began to recede. Typically, the suspended particles in the droplet are deposited on the contacting surface at the end of phase I, before the contact line breaks. Therefore, the numerical simulations reported in this paper are focused on phase I of the evaporation process.

Received: August 18, 2013

Revised: November 20, 2013

Published: February 10, 2014

Numerical simulations were conducted using FEM based software *COMSOL Multiphysics v4.3a* (COMSOL, Inc. Stockholm, Se). The governing equations and related boundary conditions are illustrated in Figure 1, where an axisymmetric

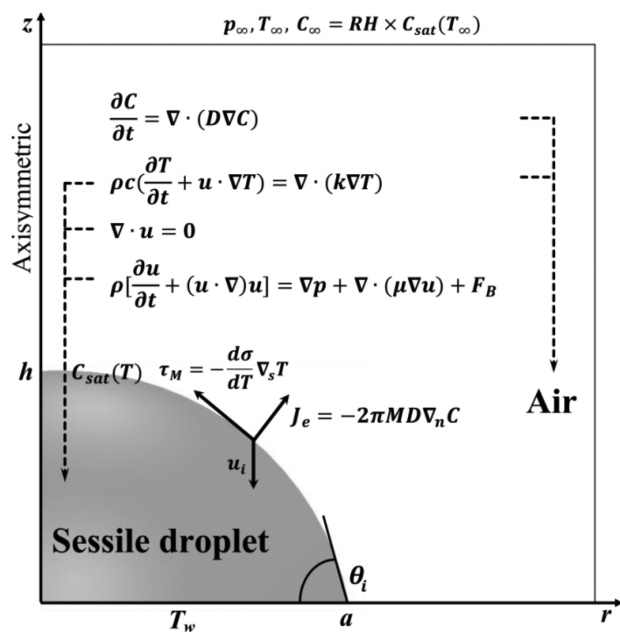


Figure 1. Computational domain: The axisymmetric droplet with initial contact angle θ_i is placed on the isothermal substrate under ambient conditions. The evaporation flux, J_e , vertical interface velocity, u_i , and Marangoni stress, τ_M , are applied on the air/liquid interface.

droplet with initial contact angle θ_i is surrounded by stationary air with specified ambient conditions. The evaporation flux, J_e , vertical interface velocity, u_i , and Marangoni stress, τ_M , are applied on the air/liquid interface. We assumed two different domains for liquid sessile droplet and stationary surrounding air with an interface defining the separation of the two domains. We utilized the arbitrary Lagrangian–Eulerian moving mesh to capture the effect of the movement of the air/liquid interface during evaporation on the internal flows within the droplet. The heat transfer and fluid dynamics equations were written in an Eulerian frame and mapped into a Lagrangian mesh. The Winslow smoothing method was utilized for calculation of deformed mesh during the evaporation. For the calculations, triangular elements with the first order discretization were employed. Various mesh sizes were assessed for mesh independency, and a mesh with 4×10^4 elements was chosen

for the simulations, corresponding to a physical spatial resolution of $10 \mu\text{m}$ inside of a $2 \mu\text{L}$ droplet.

The fluid flow in the droplet is governed by Navier–Stokes equations.

$$\nabla \cdot \mathbf{u} = 0 \quad (1)$$

$$\rho \left[\frac{\partial \mathbf{u}}{\partial t} + (\mathbf{u} \cdot \nabla) \mathbf{u} \right] = -\nabla p + \nabla \cdot (\mu \nabla \mathbf{u}) + \mathbf{F}_B \quad (2)$$

where $\mathbf{F}_B = g\beta(T - T_\infty)$ is the buoyancy force which depends on the expansion coefficient. For water $\beta = 2.07 \times 10^{-4} \text{ K}^{-1}$ at $T = 25^\circ\text{C}$. To find the temperature field in the liquid and air, the energy equation was solved for two domains.

$$\rho c \left(\frac{\partial T}{\partial t} + \mathbf{u} \cdot \nabla T \right) = \nabla \cdot (k \nabla T) \quad (3)$$

Finally, the diffusion equation in stationary air was taken into account to find the concentration of liquid vapor in air to calculate the evaporation rate and mass loss from the air/liquid interface. The buoyancy effect and subsequently convective vapor transfer from the interface were neglected in the surrounding air, which is justified as a result of the small temperature difference between the heated wall and the ambient conditions.^{30–32} The effect of the natural convection becomes significant when the temperature difference between the heated surface and the ambient is large, resulting in the faster evaporation.³³

$$\frac{\partial C}{\partial t} = \nabla \cdot (D \nabla C) \quad (4)$$

For the boundary conditions, we applied ambient conditions far from the droplet surface (T_∞ , $C_{v,\infty}$ according to the relative humidity RH), constant temperature and no slip condition on the solid surface, and saturated condition on the air/liquid interface. Therefore, the evaporation flux from the air/liquid interface is calculated from $J_e = -2\pi M D \nabla_n C$. The subscript “n” indicates the gradients perpendicular to the interface. For water, the concentration of water vapor is related to the vapor pressure of the water molecules in air by the equation of state of ideal gas as $C = p_v/RT$ where the vapor pressure of water is calculated from the Antoine equation as³⁴

$$\log_{10}(p_{v,\text{sat}} [\text{Pa}]) = A_1 + \frac{A_2}{T[\text{K}] + A_3} \quad (5)$$

where $A_1 = 8.07131$, $A_2 = -1730.63$, and $A_3 = -39.724$. On the curved interfaces, the saturation vapor pressure depends on the radius of curvature through the Kelvin equation as $\ln(p_v/p_{v,\text{sat}}) = 2\sigma M/R_p RT$. However, in our simulations, the radius of

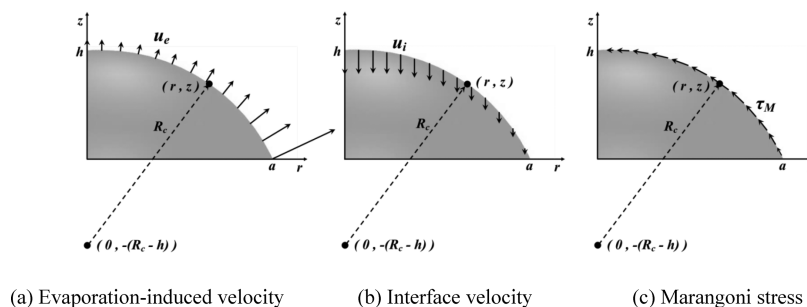


Figure 2. Velocity and Marangoni stress at the air/liquid interface. (a) Nonuniform evaporation from the interface, (b) inward velocity of the interface due to evaporation from the pinned contact line, and (c) Marangoni stress on the interface due to the temperature gradient.

Table 1. Coefficients of Variable F in the Evaporation Rate Equation: $F = F_4\theta^4 + F_3\theta^3 + F_2\theta^2 + F_1\theta + F_0$

contact angle	F_4	F_3	F_2	F_1	F_0
$\theta > 10^\circ$	1.033×10^{-2}	-8.878×10^{-2}	0.116	0.6333	8.957×10^{-5}
$\theta < 10^\circ$	0	-6.144×10^{-2}	9.591×10^{-2}	0.6366	0

curvature is large enough that the effect of the curvature is negligible. In addition, the cooling effect due to evaporation of the liquid from the interface was added to the boundary as the heat source based on evaporation flux and latent heat as $q'' = -J_e h_{fg}$, where the latent heat of vaporization h_{fg} for water is a function of temperature. To find the flow within the droplet, we applied Marangoni shear stress as the boundary condition for Navier–Stokes equations on the air/liquid interface to find the velocity field inside of the droplet. The Marangoni stress is $\tau_M = (d\sigma/dT)\nabla_s T$, where for water $d\sigma/dT = -0.1657 \times 10^{-3} \text{ N m}^{-1} \text{ K}^{-1}$. The temperature gradient along the air/liquid interface, $\nabla_s T$, was calculated to determine the Marangoni shear stress.

The sessile droplet was assumed to have the shape of a spherical cap resting on the surface. Its shape is controlled by the Bond number, $Bo = [ga^2(\rho_L - \rho_G)]/\sigma$, which accounts for the balance of surface tension and gravitational force on the droplet. For a microscale droplet, the Bond number is in the range 10^{-2} – 10^{-1} . Therefore, the droplet shape remains spherical throughout the evaporation process, which means the interface follows $f(r, z) = (R_c^2 - r^2)^{1/2} - (R_c - h)$. The interface recedes inward according to the evaporation flux calculated from the evaporation rate in each time step. However, the evaporation flux is higher near the contact line, which induces fluid flow from the apex to the contact line. The evaporation-induced velocity (\mathbf{u}_e), the vertical velocity of the interface (\mathbf{u}_i), and the Marangoni stress on the interface (τ_M) are illustrated in Figure 2.

Since the evaporation rate is higher near the contact line, the mass that is removed by the evaporation from the edge of the droplet must be replenished by a flow of liquid from the interior toward the contact line. The total fluid velocity just inside the interface is the vector summation of the interface velocity and the evaporation velocity, which results in the convective flow from the droplet apex to the contact line. The evaporation-induced velocity is calculated from the evaporation rate as

$$\mathbf{u}_e = -\frac{J_e}{\rho} = -\frac{2\pi MD}{\rho} \nabla_n C \quad (6)$$

The interface velocity is inward and vertical due to the pinned contact line and calculated from the time derivative of the interface formula by

$$\mathbf{u}_i = -\frac{df(r, z)}{dt} = -\frac{df(r, z)}{dR_c} \frac{dR_c}{dt} - \frac{df(r, z)}{dh} \frac{dh}{dt} \quad (7)$$

The droplet volume, $V = (\pi h/6)(3a^2 + h^2)$, and radius of curvature, $R_c = (h/2) + (a^2/2h)$ of the spherical droplet depend on the droplet height, h , and constant contact line radius, a . Therefore,

$$\frac{dh}{dt} = \frac{\frac{dV}{dt}}{\frac{\pi}{2}(a^2 + h^2)}, \quad \frac{dR_c}{dt} = \frac{1}{2} \left(1 - \frac{a^2}{h^2} \right) \frac{\frac{dV}{dt}}{\frac{\pi}{2}(a^2 + h^2)} \quad (8)$$

Finally, from the analytical expression for the interface,

$$\frac{df(r, z)}{dR_c} = R_c(R_c^2 - r^2)^{-1/2} - 1, \quad \frac{df(r, z)}{dh} = 1 \quad (9)$$

The evaporation rate is calculated by the integration of evaporation flux on the air/liquid interface as

$$\frac{dV}{dt} = -\frac{J_e}{\rho} = -\int \frac{2\pi r MD}{\rho} \nabla_n C \, dl \quad (10)$$

All the governing equations were solved simultaneously assuming temperature-dependent physical and thermodynamic properties for water and air.^{35,36}

In the case of slow evaporation of a spherical droplet on the surface in still air, Picknett and Bexon calculated the rate of evaporation on the basis of the diffusion equation. We employed their results to validate our numerical method. They assumed that the evaporation rate is defined as

$$\frac{dV}{dt} = -\frac{2\pi D \Delta C}{\rho} F \left(\frac{3V}{\pi G} \right)^{1/3} \quad (11)$$

where $\Delta C = C_{\text{sat}} - C_\infty$ is the difference between the water vapor concentration on the droplet surface and the bulk. Two variables F and G are dependent on droplet contact angle during the evaporation as

$$F = F_4\theta^4 + F_3\theta^3 + F_2\theta^2 + F_1\theta + F_0 \quad (12)$$

$$G = (1 - \cos \theta)^2 (2 + \cos \theta) \quad (13)$$

where the contact angle θ is in radians. The coefficients are listed in Table 1.

Equation 11 was solved numerically for the droplet with pinned contact line to find the total evaporation time. The contact angle during evaporation changes according to the height and radius of the curvature of the droplet. Since the contact line radius, a , is assumed constant during evaporation, the height of the droplet and radius of curvature are calculated as

$$\frac{\pi}{6} h^3 + \frac{\pi}{2} a^2 h - V = 0 \rightarrow h \rightarrow R_c = \frac{a^2 + h^2}{2h} \quad (14)$$

Therefore, the contact angle during evaporation becomes

$$\theta = \frac{\pi}{2} - \sin^{-1} \left(\frac{R_c - h}{R_c} \right) \quad (15)$$

This is used to find the evaporation rate and consequently the total evaporation time.

■ DIMENSIONAL SCALING

To find a general correlation for the evaporation time, we scaled the variables and made the equations dimensionless. We scaled the length with the contact line radius, a , and the velocity with the evaporation-induced velocity, U ,

Table 2. Important Dimensionless Numbers for Droplet Evaporation

number	equation	range	importance
bond	$B_o = \frac{ga^2(\rho_L - \rho_G)}{\sigma}$	10^{-2} – 10^{-1}	the droplet shape remains spherical during evaporation
diffusion Péclet	$Pe_D = \frac{Ua}{D}$	0 – 10^{-2}	the evaporation is dominated by the diffusion of liquid vapor into air
Marangoni	$Mg = -\frac{d\sigma}{dT} \frac{a\Delta T}{\mu\alpha}$	10^{-4} – 10^{-1}	in the presence of a surface tension gradient, the internal flow is dominated by Marangoni flow
Rayleigh	$Ra = \frac{g\beta(T_w - T_\infty)a^3}{\alpha\nu}$	10^{-1} – 10^1	the buoyancy force inside of the droplet is not important except at very high wall temperatures
Reynolds	$Re = \frac{Ua}{\nu}$	10^{-3} – 10^{-1}	the inertia is negligible within the droplet
thermal Péclet	$Pe_T = \frac{Ua}{\alpha}$	10^{-5} – 10^{-2}	the heat transfer is dominated by thermal diffusion

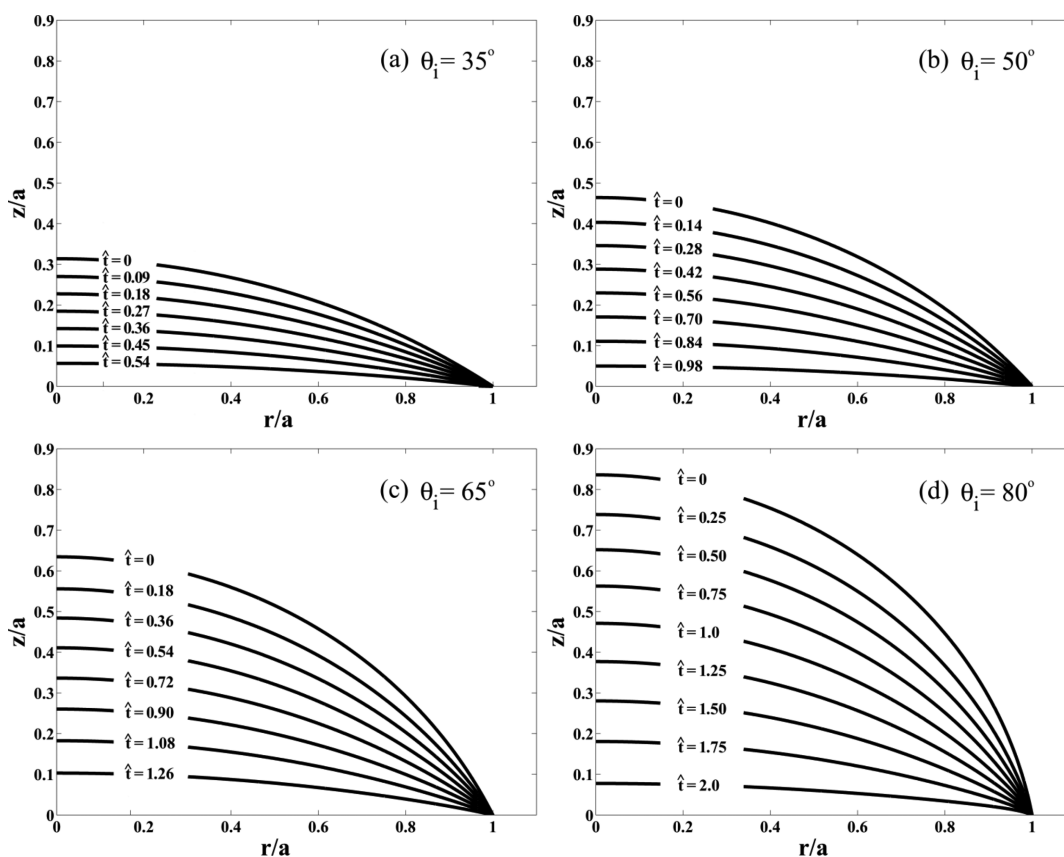


Figure 3. Droplet profiles at different dimensionless times for evaporation of a droplet with initial contact angles (a) $\theta_i = 35^\circ$, (b) $\theta_i = 50^\circ$, (c) $\theta_i = 65^\circ$, and (d) $\theta_i = 80^\circ$.

$$\hat{u} = \frac{u}{U}, \quad \hat{t} = \frac{tU}{a}, \quad \hat{p} = \frac{p}{\rho U^2}, \quad \hat{T} = \frac{T - T_\infty}{T_w - T_\infty},$$

$$\hat{C} = \frac{C - C_\infty}{C_{\text{sat}} - C_\infty} \quad (16)$$

where the evaporation-induced velocity depends on the evaporation rate as

$$U = \frac{2\pi MD(C_{\text{sat}} - C_\infty)}{\rho a} \quad (17)$$

The dimensionless governing equations, by dropping the hat, become

$$\nabla \cdot \mathbf{u} = 0 \quad (18)$$

$$\frac{\partial \mathbf{u}}{\partial t} + (\mathbf{u} \cdot \nabla) \mathbf{u} = -\nabla p + \frac{1}{Re} \nabla^2 \mathbf{u} + \frac{a}{\rho U^2} \mathbf{F}_B \quad (19)$$

$$\frac{\partial T}{\partial t} + \mathbf{u} \cdot \nabla T = \frac{1}{Pe_T} \nabla^2 T \quad (20)$$

$$\frac{\partial C}{\partial t} = \frac{1}{Pe_C} \nabla^2 C \quad (21)$$

Table 2 shows the relevant dimensionless numbers, along with their characteristic values, that govern the physics of droplet evaporation. These numbers are estimated on the basis

of the following: droplet volume $V = 0.5\text{--}5\ \mu\text{L}$, droplet radius of contact line $a = 0.5\text{--}2\ \text{mm}$, liquid density $\rho_L = 998\ \text{kg m}^{-3}$, air density $\rho_G = 1.2\ \text{kg m}^{-3}$, surface tension $\sigma_0 = 0.072\ \text{N m}^{-1}$ at $T_\infty = 298\ \text{K}$, diffusion of water vapor into air $D = 2.45 \times 10^{-5}\ \text{m}^2\ \text{s}^{-1}$,³⁷ surface tension gradient $d\sigma/dT = -10^{-4}$ to $-10^{-8}\ \text{N m}^{-1}\ \text{K}^{-1}$, temperature difference on the air/liquid interface $\Delta T = 0\text{--}0.5\ \text{K}$, kinematic viscosity $\mu = 10^{-3}\ \text{Pa s}$, thermal diffusivity of water $\alpha = 1.43 \times 10^{-5}\ \text{m}^2\ \text{s}^{-1}$, thermal expansion of water $\beta = 2 \times 10^{-4}\ \text{K}^{-1}$, relative humidity $\text{RH} = 10\text{--}90\%$, wall temperature $T_w = 298\text{--}313\ \text{K}$, ambient temperature $T_\infty = 298\ \text{K}$, and dynamic viscosity $\nu = 10^{-6}\ \text{m}^2\ \text{s}^{-1}$. According to these typical values, the range of the evaporation-induced velocity is $U = 10^{-1}\text{--}10^2\ \mu\text{m s}^{-1}$ and the Marangoni velocity is $U_{Mg} = 0\text{--}0.2\ \text{cm s}^{-1}$.

The dimensionless evaporation time was defined as

$$\hat{t}_e = \frac{U}{a} t_e = \frac{2\pi MD(C_{\text{sat}} - C_\infty)}{\rho a^2} t_e \quad (22)$$

Using this dimensional scaling, we demonstrate that the dimensionless evaporation time only depends on the droplet initial contact angle and a general correlation is proposed.

RESULTS AND DISCUSSION

The time evolution of the droplet during evaporation is illustrated in Figure 3 for a droplet with initial contact angles of $\theta_i = 35, 50, 65$, and 80° .

The evaporation rate $J_e = -2\pi MD\nabla_n C$ is approximately constant throughout the evaporation process. Therefore, the droplet volume decreases nearly linear in time, as shown in Figure 4a. The evaporation rate becomes slightly nonlinear for higher contact angles as a result of the evaporation from the non-isothermal interface. The gradient of the vapor concentration on the interface ($\nabla_n C$) scales with the temperature difference between the air/liquid interface and the ambient conditions. At low contact angles, the temperature of the interface is almost constant and close to the wall temperature, resulting in constant evaporation rate. However, at higher contact angles, the temperature of the interface becomes nonuniform, resulting in a slightly nonlinear evaporation rate.

The contact line of the droplet is pinned, implying that the contact radius is constant throughout the evaporation; meanwhile, the droplet height and contact angle decrease in time, as shown in Figure 4b and c. It continues until the breakage of the pinned contact line, where the contact line recedes at constant contact angle. All the results are for a droplet with initial contact angles of $\theta_i = 35, 50, 65$, and 80° .

We assumed that the evaporation time is proportional to $V^{2/3}$.³⁸ The dimensionless volume is

$$\hat{V} = \frac{\frac{\pi h}{6}(3a^2 + h^2)}{a^3} = \frac{\pi}{2}\left(\frac{h}{a}\right) + \frac{\pi}{6}\left(\frac{h}{a}\right)^3 \quad (23)$$

From the geometrical calculations, the ratio of the droplet height and contact line radius depends only upon the contact angle as

$$a^2 = 2R_c h - h^2 \rightarrow \frac{h}{a} + \frac{a}{h} = \frac{2}{\sin(\theta)} \quad (24)$$

Therefore, the dimensionless volume only depends on the contact angle and consequently the correlation for the dimensionless evaporation time can be reduced to only a function of the initial contact angle as

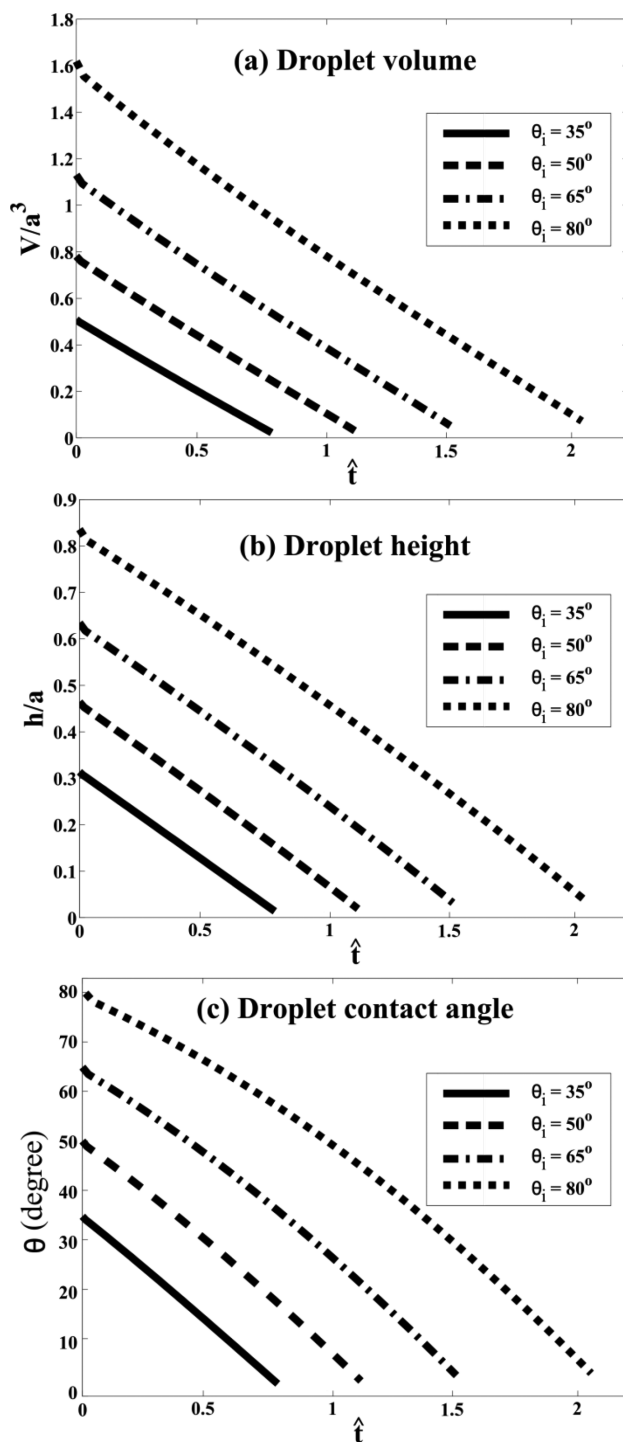


Figure 4. Time evolution of (a) droplet volume, (b) droplet height, and (c) droplet contact angle during evaporation of a droplet with initial contact angle $\theta_i = 35, 50, 65$, and 80° .

$$\hat{t}_e = (B_4\theta_i^4 + B_3\theta_i^3 + B_2\theta_i^2 + B_1\theta_i + B_0)\hat{V}^{2/3} \quad (25)$$

where the constants are shown in Table 3 for the initial contact angle.

Figure 5 shows the comparison between the proposed correlation and the results from different experimental and numerical results reported by Picknett and Bexon, Hu and Larson, and Schönfeld et al. The relative error between the correlation and other results is less than 1% for a range of

Table 3. Coefficients of the Correlation for the Dimensionless Evaporation Time: $\hat{t}_e = (B_4\theta_i^4 + B_3\theta_i^3 + B_2\theta_i^2 + B_1\theta_i + B_0)\hat{V}^{2/3}$

contact angle	B_4	B_3	B_2	B_1	B_0
θ_i (rad)	-0.234	1.037	-1.754	1.8	0.531
θ_i (deg)	-2.17×10^{-8}	5.51×10^{-6}	-5.34×10^{-4}	3.14×10^{-2}	0.531

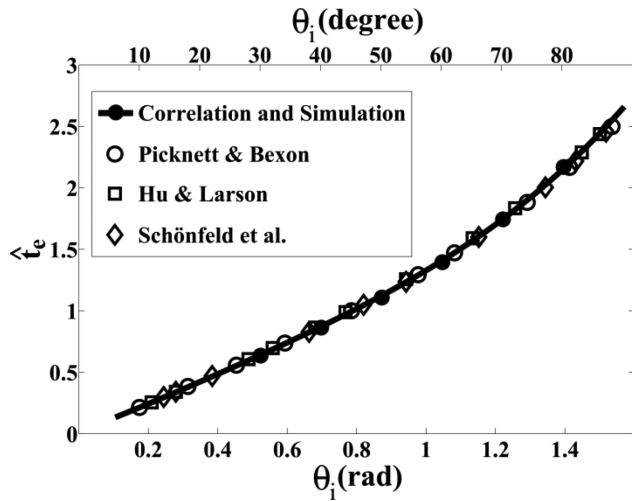


Figure 5. Comparison between the proposed correlation for dimensionless evaporation time as $\hat{t}_e = (B_4\theta_i^4 + B_3\theta_i^3 + B_2\theta_i^2 + B_1\theta_i + B_0)\hat{V}^{2/3}$ with the current numerical simulation and other published experimental and numerical results.

temperatures from $T_w = 298$ to 313 K, volume from 0.1 to $5 \mu\text{L}$, and contact angle from 10 to 85° .

In this section, we consider the internal flow within the droplet during evaporation for three Marangoni numbers, $Mg = 10^{-4}$, 10^{-3} , and 10^{-1} . Figure 6 depicts the internal flow as a result of Marangoni stress and evaporation for a droplet with initial contact angle $\theta_i = 80^\circ$. In this example, we chose a contact line radius $a = 1.07$ mm, wall temperature $T_w = 313$ K, ambient temperature $T_\infty = 298$ K, and relative humidity $RH = 30\%$, which means that the characteristic evaporation-induced velocity becomes $U \approx 7 \mu\text{m s}^{-1}$. Figure 6 shows the velocity within the droplet scaled by the Marangoni velocity, $U_{Mg} = (Mg\alpha)/a$, which varies from $U_{Mg} = 1.4 \mu\text{m s}^{-1}$ for $Mg = 10^{-4}$ (Figure 6a), $14 \mu\text{m s}^{-1}$ for $Mg = 10^{-3}$ (Figure 6b), and $U_{Mg} = 1.4 \text{ mm s}^{-1}$ for $Mg = 10^{-1}$ (Figure 6c). In Figure 6b, the Marangoni velocity scale is comparable to the evaporation velocity scale, which occurs when

$$U_{Mg} \cong U \rightarrow \frac{Mg\alpha}{a} \cong \frac{2\pi MD(C_{\text{sat}} - C_\infty)}{\rho a} \rightarrow Mg \cong \frac{2\pi MD(C_{\text{sat}} - C_\infty)}{\rho \alpha} \quad (26)$$

Figure 6a represents the case when the Marangoni velocity is much smaller than the evaporation velocity scale $U_{Mg} \ll U$, while in Figure 6c it is much larger, $U_{Mg} \gg U$. At small Marangoni number $Mg = 10^{-4}$ (Figure 6a), the circulating velocity within the droplet is negligible and there is no

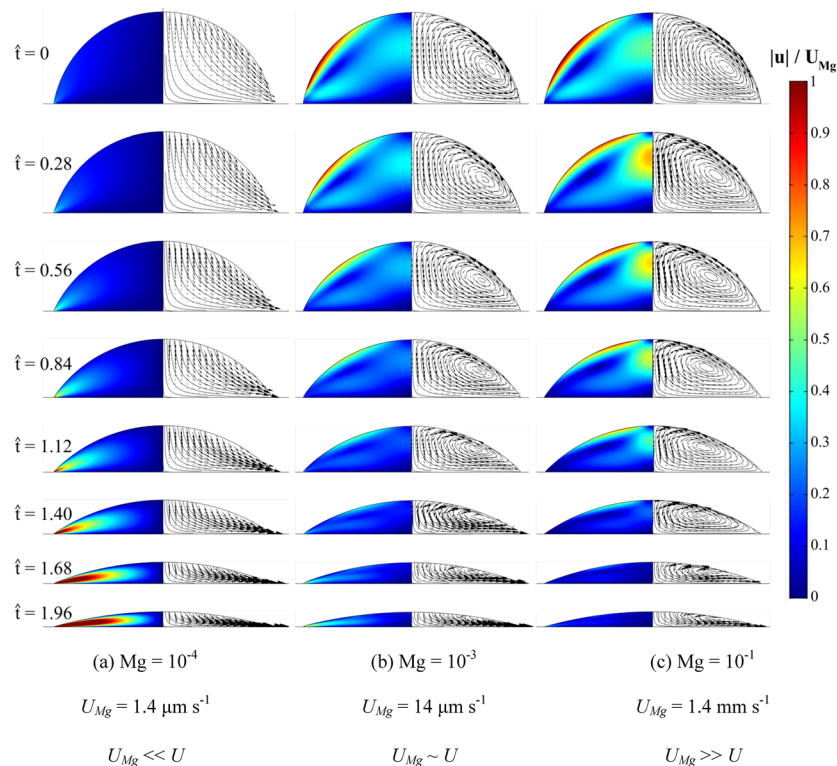


Figure 6. Evaporation of the droplet and internal flows as a result of Marangoni stresses and evaporation from the pinned contact line for initial contact angle $\theta_i = 80^\circ$ and for different Marangoni numbers (a) $Mg = 10^{-4}$, (b) $Mg = 10^{-3}$, and (c) $Mg = 10^{-1}$. The velocity within the droplet is normalized with Marangoni velocity, $U_{Mg} = Mg\alpha/a$. The characteristic evaporation velocity is $U = 7 \mu\text{m s}^{-1}$ for all of the cases.

significant convective mixing for $\hat{t} < 1$. For later times, $\hat{t} > 1$, the droplet height becomes sufficiently small and an evaporation-driven jet-like flow develops and ejects fluid toward the contact line which scales with the evaporation velocity U . At higher Marangoni numbers, $Mg = 10^{-3}$ (Figure 6b) and $Mg = 10^{-1}$ (Figure 6c), the Marangoni velocity is sufficiently large, providing an excellent convective mixing, for $\hat{t} < 1$. For later times, $\hat{t} > 1.4$, the same evaporation-driven jet-like flow ejects fluid toward the contact line. This evaporation-driven flow occurs in all cases but is not readily observable for the highest Marangoni number when the velocity is scaled by Marangoni velocity (see Figure 6c).

Toward the end of phase I of the droplet evaporation, the temperature gradient and subsequently the Marangoni flow nearly vanish, just before the contact line breaks. In all cases, the evaporation-induced velocity carries all the species within the droplet to the perimeter, forming the coffee ring stain at the end of the evaporation. Figure 7 illustrates the spatially

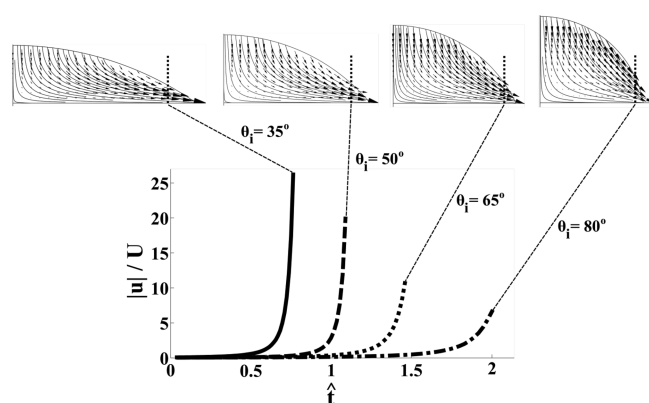


Figure 7. The average evaporation-induced velocity of droplets with different contact angles near the contact line at $r/a = 0.9$, for varying initial contact angles of $\theta_i = 35$, 50, 65, and 80° .

averaged velocity near the contact line throughout the evaporation process, independent of the Marangoni number, for the initial contact angles of $\theta_i = 35$, 50, 65, and 80° . The velocity field was scaled by the evaporation-induced velocity, U . The fluid velocity reaches its maximum near the end of the evaporation process, and creates a jet-like flow toward the contact line just before the contact line breaks. Since the mass loss due to evaporation is nearly constant throughout the evaporation process, the decreasing droplet height requires that the velocity increases in order to maintain an approximately constant outgoing evaporation flux. Smaller initial contact angles lead to higher nondimensional velocities, just before the contact line breaks. The velocities reach a maximum of $u/U = 25$, 20, 10, and 7 for $\theta_i = 35$, 50, 65, and 80° , respectively.

DISCUSSION AND CONCLUSIONS

Numerical simulations were conducted to quantify the evaporation rate of sessile droplets with pinned contact line on isothermal surfaces. The rate of evaporation is nearly constant throughout the evaporation process. Early in the evaporation process, thermal gradients along the air/liquid interface create Marangoni-induced flow that can stir the droplet and provide a significant convective mixing within the droplet, depending upon the Marangoni number. As the droplet volume decreases, the thermal gradients become

smaller and the Marangoni-induced flow becomes negligible. Simultaneously, the decreased droplet height creates an outward large jet-like flow toward the contact line. The jet-like flow dominates droplet fluid motion during the late stages of evaporation, and is responsible for the so-called coffee ring stain formation. For a droplet with an initial contact angle of $\theta_i = 80^\circ$, the transition between Marangoni-dominated flow and evaporation-dominated flow occurs around $\hat{t} < 1-1.4$, depending upon the Marangoni numbers.

The internal fluid motion is important for transport of particulate matter that exhibits low diffusivities, and leads to the coffee ring stain. The thermal diffusivity is sufficiently large that the thermal Péclet number is relatively low for the conditions considered in the current study. Therefore, the heat transfer and consequently the evaporation rate are nearly constant and independent of the internal fluid motion. As a result, we reported a simple correlation for the dimensionless evaporation time for a droplet with pinned contact line as a function of contact angle, $\hat{t}_e = (B_4\theta_i^4 + B_3\theta_i^3 + B_2\theta_i^2 + B_1\theta_i + B_0)\hat{V}^{2/3}$, which is in accord with the previous experimental and numerical results.

AUTHOR INFORMATION

Corresponding Author

*Phone: (805) 893-4563, E-mail: meinhart@engineering.ucsb.edu.

Notes

The authors declare no competing financial interest.

ACKNOWLEDGMENTS

This work was supported by the Institute for Collaborative Biotechnologies through grant W911NF-09-0001 from the U.S. Army Research Office. The content of the information does not necessarily reflect the position or the policy of the Government, and no official endorsement should be inferred.

NOMENCLATURE

C (mol m^{-3})	concentration
θ (deg)	contact angle
ρ (kg m^{-3})	density
D ($\text{m}^2 \text{s}^{-1}$)	diffusion coefficient
h (m)	droplet height
a (m)	droplet radius of contact line
A (m^2)	droplet surface area
V (m^3)	droplet volume
μ (Pa s)	dynamic viscosity
J_e (kg s^{-1})	evaporation rate
β (K^{-1})	expansion coefficient
F_B (N)	buoyancy force
R ($\text{J mol}^{-1} \text{K}^{-1}$)	gas constant
g (m s^{-2})	gravity acceleration
c ($\text{J kg}^{-1} \text{K}^{-1}$)	heat capacitance
θ_i (deg)	initial contact angle
ν ($\text{m}^2 \text{s}^{-1}$)	kinematic viscosity
M (kg mol^{-1})	molecular weight
p_v (Pa)	partial pressure of liquid vapor
p (Pa)	pressure
R_c (m)	radius of curvature
RH (%)	relative humidity
σ (N m^{-1})	surface tension
T (K)	temperature
k ($\text{W m}^{-1} \text{K}^{-1}$)	thermal conductivity

α ($\text{m}^2 \text{s}^{-1}$) thermal diffusivity
 u (m s^{-1}) velocity field

Non-Dimensional Variables

Bo bond number
 Pe_D diffusion Péclet number
 Mg Marangoni number
 Ra Rayleigh number
 Re Reynolds number
 Pe_T thermal Péclet number

Subscripts and Superscripts

e evaporation
 i interface
 n normal to surface
 ∞ surrounding
 v vapor
 w wall
 sat saturation

REFERENCES

- (1) Dugas, V.; Broutin, J.; Souteyrand, E. Droplet Evaporation Study Applied to DNA Chip Manufacturing. *Langmuir* **2005**, *21*, 9130–9136.
- (2) Ortiz, C.; Zhang, D.; Xie, Y.; Ribbe, A. E.; Ben-Amotz, D. Validation of the Drop Coating Deposition Raman Method for Protein Analysis. *Anal. Biochem.* **2006**, *353*, 157–166.
- (3) Filik, J.; Stone, N. Drop Coating Deposition Raman Spectroscopy of Protein Mixtures. *Analyst* **2007**, *132*, 544–550.
- (4) Jia, W.; Qiu, H. H. Experimental Investigation of Droplet Dynamics and Heat Transfer in Spray Cooling. *Exp. Therm. Fluid Sci.* **2003**, *27*, 829–838.
- (5) Brinker, C. J.; Lu, Y.; Sellinger, A.; Fan, H. Evaporation-Induced Self-Assembly: Nanostructures Made Easy. *Adv. Mater.* **1999**, *11*, 579–585.
- (6) Marín, Á.; Gelderblom, H.; Lohse, D.; Snoeijer, J. Order-to-Disorder Transition in Ring-Shaped Colloidal Stains. *Appl. Phys. Lett.* **2011**, *107*, 085502.
- (7) Small, W. R.; Walton, C. D.; Loos, J.; Panhuis, M. Carbon Nanotube Network Formation from Evaporating Sessile Drops. *J. Phys. Chem. B* **2006**, *110*, 13029–13036.
- (8) Barmi, M. R.; Andreou, C.; Hoonejani, M. R.; Moskovits, M.; Meinhart, C. D. Aggregation Kinetics of SERS-Active Nanoparticles in Thermally Stirred Sessile Droplet. *Langmuir* **2013**, *29*, 13614–13623.
- (9) Deegan, R.; Bakajin, O.; Dupont, T.; Huber, G.; Nagel, S. R.; Whitten, T. A. Capillary Flow as the Cause of Ring Stains from Dried Liquid Drops. *Nature* **1997**, *389*, 827–829.
- (10) Bhardwaj, R.; Fang, X.; Attinger, D. Pattern Formation During the Evaporation of a Colloidal Nanoliter Drop: a Numerical and Experimental Study. *New J. Phys.* **2009**, *11*, 075020.
- (11) Widjaja, E.; Harris, M. Particle Deposition Study During Sessile Drop Evaporation. *AIChE J.* **2008**, *54*, 2250–2260.
- (12) Fischer, B. Particle Convection in an Evaporating Colloidal Droplet. *Langmuir* **2002**, *18*, 60–67.
- (13) Birdi, K. S.; Vu, D. T. A Study of the Evaporation Rates of Small Water Drops Placed on a Solid Surface. *J. Phys. Chem.* **1989**, *93*, 3102–3703.
- (14) Saada, M.; Chikh, S.; Tadrist, L. Numerical Investigation of Heat and Mass Transfer of an Evaporating Sessile Drop on a Horizontal Surface. *Phys. Fluids* **2010**, *22*, 112115.
- (15) Shahidzadeh-Bonn, N.; Rafai, S.; Azouni, A.; Bonn, D. Evaporating Droplets. *J. Fluid Mech.* **2006**, *549*, 307–314.
- (16) Barash, L.; Bigoni, T.; Vinokur, V.; Shchur, L. Evaporation and Fluid Dynamics of a Sessile Drop of Capillary Size. *Phys. Rev. E* **2009**, *79*, 046301.
- (17) Lorenzini, G.; Saro, O. Thermal Fluid Dynamic Modeling of a Water Droplet Evaporating in Air. *Int. J. Heat Mass Transfer* **2013**, *62*, 323–335.
- (18) Sodtke, C.; Ajaev, V.; Stephan, P. Dynamics of Volatile Liquid Droplets on Heated Surfaces: Theory Versus Experiment. *J. Fluid Mech.* **2008**, *610*, 343–362.
- (19) McHale, G.; Aqil, S.; Shirtcliffe, N.; Newton, M.; Erbil, H. Analysis of Droplet Evaporation on a Superhydrophobic Surface. *Langmuir* **2005**, *21*, 11053–11060.
- (20) Trybala, A.; Okoye, A.; Semenov, S.; Agogo, H.; Rubio, R. G.; Ortega, F.; Starov, V. M. Evaporation Kinetics of Sessile Droplets of Aqueous Suspensions of Inorganic Nanoparticles. *J. Colloid Interface Sci.* **2013**, *403*, 49–57.
- (21) Picknett, R. G.; Bexon, R. The Evaporation of Sessile or Pendant Drops in Still Air. *J. Colloid Interface Sci.* **1977**, *61*, 336–350.
- (22) Hu, H.; Larson, R. Evaporation of a Sessile Droplet on a Substrate. *J. Phys. Chem. B* **2002**, *106*, 1334–1344.
- (23) Schönfeld, F.; Graf, K. H.; Hard, S.; Butt, H. J. Evaporation Dynamics of Sessile Liquid Drops in Still Air with Constant Contact Radius. *Int. J. Heat Mass Transfer* **2008**, *51*, 3696–3699.
- (24) Xu, X.; Luo, J. Marangoni Flow in an Evaporating Water Droplet. *Appl. Phys. Lett.* **2007**, *91*, 124102.
- (25) Hu, H.; Larson, R. Analysis of the Effects of Marangoni Stresses on the Microflow in an Evaporating Sessile Droplet. *Langmuir* **2005**, *21*, 3972–3980.
- (26) Petsi, A.; Burganos, V. Potential Flow Inside an Evaporating Cylindrical Line. *Phys. Rev. E* **2005**, *72*, 047301.
- (27) Tarasevich, Y. Simple Analytical Model of Capillary Flow in an Evaporating Sessile Drop. *Phys. Rev. E* **2005**, *71*, 027301.
- (28) Petsi, A.; Burganos, V. Stokes Flow inside an Evaporating Liquid Line for Any Contact Angle. *Phys. Rev. E* **2008**, *78*, 036324.
- (29) Panwar, A. K.; Barthawal, S. K.; Ray, S. Effect of Evaporation on the Contact Angle of a Sessile Drop on Solid Substrates. *J. Adhes. Sci. Technol.* **2003**, *17*, 1321–1329.
- (30) Girard, F.; Antoni, M.; Sefiane, K. On the Effect of Marangoni Flow on Evaporation Rates of Heated Water Drops. *Langmuir* **2008**, *24*, 9207–9210.
- (31) Girard, F.; Antoni, M.; Faure, S.; Steinchen, A. Evaporation and Marangoni Driven Convection in Small Heated Water Droplets. *Langmuir* **2006**, *22*, 11085–11091.
- (32) Nguyen, T. A. H.; Nguyen, A. V.; Hampton, M. A.; Xu, Z. P.; Huang, L.; Rudolph, V. Theoretical and Experimental Analysis of Droplet Evaporation on Solid Surfaces. *Chem. Eng. Sci.* **2012**, *69*, 522–529.
- (33) Carle, F.; Sobac, B.; Brutin, D. Experimental Evidence of the Atmospheric Convective Transport Contribution to Sessile Droplet Evaporation. *Appl. Phys. Lett.* **2013**, *102*, 061603.
- (34) Thomson, G. W. The Antoine Equation for Vapor-Pressure Data. *Chem. Rev.* **1946**, *38*, 1–39.
- (35) Sonntag, R. E.; Borgnakke, C.; Van Wylen, G. J. *Fundamentals of Thermodynamics*, 7th ed.; John Wiley & Sons: Hoboken, NJ, 2009.
- (36) Incropera, F. P.; Dewitt, D. P.; Bergman, T. L.; Lavine, A. S. *Fundamentals of Heat and Mass Transfer*, 7th ed.; John Wiley & Sons: Hoboken, NJ, 2011.
- (37) Massman, W. J. A Review of the Molecular Diffusivities of H_2O , CO_2 , CH_4 , CO , O_3 , SO_2 , NH_3 , N_2O , NO , and NO_2 in air, O_2 and N_2 near STP. *Atmos. Environ.* **1998**, *32*, 1111–1127.
- (38) Houghton, H. G. A Study of the Evaporation of Small Water Drops. *Physics* **1933**, *4*, 419–424.